A modified abstraction of Sierpiński fractals towards enhanced sensitivity of a cross-coupled bow-tie nanostructure

NANO FUTURES

PAPER

A modified abstraction of Sierpiński fractals towards enhanced sensitivity of a cross-coupled bow-tie nanostructure

Dihan Hasan[1,2,3] **and Chengkuo Lee**[1,2,3]

[1] Department of Electrical & Computer Engineering, National University of Singapore, 4 Engineering Drive 3, Singapore 117576
[2] Center for Intelligent Sensors and MEMS, National University of Singapore, 4 Engineering Drive 3, Singapore 117576
[3] NUS Suzhou Research Institute (NUSRI), Suzhou Industrial Park, Suzhou, People's Republic of China 215123

E-mail: elelc@nus.edu.sg

RECEIVED
17 February 2018

REVISED
3 April 2018

ACCEPTED FOR PUBLICATION
13 April 2018

PUBLISHED
17 May 2018

Keywords: bow-tie, cross-coupling, fractal, optical magnetism, Sierpiński

Supplementary material for this article is available online

Abstract

We experimentally demonstrate a modified abstraction of a fractal geometry (up to order M = 2), namely the Sierpiński fractal, with intrinsic self-similarity for a multitude of infrared sensing applications. The modification particularly strengthens the dipolar resonance and enables optical magnetism at longer wavelengths on a relatively miniaturized footprint. In contrast to the conventional resonant sensing, we harness the broadband electric field enhancement of the modified fractal patterns originating from the lightning rod effect in the non-resonant regime. We demonstrate strong enhancement of molecular absorption at mid-IR by the fractal patterns in the non-resonant regime even under extreme thermal broadening. Finally, we extend the work towards the functional study of the molecular fingerprint of ultra-thin film (~5 nm) on a non-complementary metamaterial platform in the non-resonant regime. With the help of the solid state chemical dewetting of the monolayer, we also successfully demonstrate a new type of cross-coupling mediated sensitivity of the multispectral and mutually coupled fractal patterns. The research clearly indicates the usefulness of broadband electric field enhancement by the second order fractal pattern for on chip, complete profiling of mid-IR fingerprints of biological elements, i.e. cell, and protein monolayer on a limited footprint and under versatile morphological states.

1. Introduction

The concept of fractals is popular in microwave and radio frequency antenna designs due to the property of self-similarity that yields broadband multi-frequency responses and miniaturizes the antenna footprint for ultra-compact portable applications [1]. Fractal electromagnetism has become an interesting research topic, not only in radio frequency applications but also at optical length scale due to the precisely defined mathematical model and scalable properties of the fractals [2]. Moreover, fractal patterns are potentially useful for manipulation of surface plasmons, the oscillation of conduction band electrons in metals, for sensing, telecom and energy harvesting applications [3–10]. Various shapes of fractal nanostructures have already been exploited for sub-diffraction focusing [11], transparent metallic electrodes [12], photovoltaic efficiency enhancement [13], molecular fluorescence and surface enhanced Raman spectroscopy enhancement [14], broadband light trapping [15] and lately, multimodal broadband resonances [16]. The Sierpiński fractal is an equilateral triangular shaped fractal model with a characteristic Haudsoff dimension of $\log_2 3$ and is particularly suitable for merging with bow-tie nanostructures [17]. Among the various categories of the state-of-the-art nanostructures reported so far to manipulate localized surface plasmon resonance (LSPR), bow-tie architecture holds a unique position because of its giant field enhancement partially aided by the lightning rod effect at the sharp tips. It has been used as the key element for many high performance plasmonic applications such as nanolithography [18], ultra-low power optical trapping [19], single molecule fluorescence detection [20], extreme UV generation [21] and plasmonic photography film

for high density storage [22]. Previously, polarization dependent improvement of electric field intensity has been demonstrated in a pure Sierpiński antenna at near-IR (NIR) wavelengths (1200–2400 nm) [23]. In reality, however, it is challenging to implement a pure Sierpiński fractal due to the geometric singularity at the acute junctions of the fractal components and fabrication imperfections. Furthermore, previous research did not exploit the strong tuning mechanism of the redistribution of surface charges in bow-tie nano-triangles due to the lightning rod effect [24]. Conversely, with the help of advanced electron beam lithography, we exploit the phenomenon as a new route for precise geometric tuning of the densely spaced nanostructures. We particularly aim at an improved architecture with multispectral and strongly interacting properties at mid-IR (3000–8000 nm) range that possesses completely different resonance characteristics compared to the previous research and above all preserves optical magnetism. On the contrary, the polarization independent arrangement of the components is implemented to maximize the lightning rod effect of the fractal patterns in the non-resonant regime. We provide the proof-of-concept of the improvement by demonstrating strong enhancement of molecular absorptions in the non-resonant regime even under extreme thermal broadening. Together with the aforementioned unique properties of the new nano-architectures, here, we successfully demonstrate non-resonant detection of a weak molecular fingerprint of a chemically unstable ultra-thin film (~5 nm) for the first time in the literature. With the aid of solid state dewetting of the monolayer at room temperature, we further report a novel cross-coupling mediated sensing mechanism for morphological transformation of the film over time on the fractal platform.

2. Design approach and physics

2.1. Design details

In figures 1(a), (b) and (c), we show the evolution of Sierpiński fractal surfaces of order 1 and order 2 from the host equilateral triangle. A pattern of a given order is generated by subdividing the remaining triangles into four smaller congruent triangles while removing the center one. Note that, the solid triangular components of an ideal fractal antenna touch each other at a single point, which is why a collective excitation of all the components cannot be possible due to the geometric singularity. Such singularity is also not possible to achieve by the state-of-the-art patterning techniques. Figure 1 depicts the chronological development of the modified abstraction considered in this work. In figures 1(k) and (l), we show the polarization independent cross-coupled configurations of two different orders (M1 and M2) of fractalized devices on oxide coated substrate. Here, the modified fractal triangle constitutes one of the four arms of the cross-coupled patterns. We provide the parameter: offset (f) not only to avoid the geometric singularities in simulation and fabrication, but also to exploit the strong impact of lightning rod derived surface currents on the resonance properties. We further provide the split gap (s) in order to achieve a dramatic enhancement of resonance contrast and optical magnetism in mid-IR as discussed in the following sections. Note that, through such a modified fractalization process with recursively changing Haudsoff dimension, we still achieve the coherently coupled self-symmetric radiators as numbered in figures 1(i) and 2(j). The height of each host triangle is kept constant at 1.225 μm, roughly calculated from the half-wavelength dipole equation defined as $\lambda/2 = L$, where L is the total length of the dipole under a given polarization. Please note that, due to the cross-coupled arrangement, the resonance characteristics of the patterns do not critically depend on the polarization, albeit the profiles of the near field enhancement can differ.

2.2. Fabrication

The structures are written by high resolution 100 KV ELS-7000 electron beam lithography equipment using raster scanning. The e-beam current is maintained at 200 pA. No proximity correction or ITO charge compensation layer has been considered for the current batch of chips. Thus, the issue of backscattering induced corner roundedness may be crucial in some cases. The development time is controlled at 70 s in 1:3 MIBK:IPA solution. Finally, 5 nm of Cr layer followed by 35 nm of gold layer has been deposited at a rate of 1 angstrom/sec by the Denton Explorer e-beam evaporator while maintaining the vacuum level at 5e-7 torr. The metal lift off has been performed by soaking the samples in acetone solution overnight followed by 5 min long ultrasonic agitation. Figure 2(a) shows the field emission scanning electron microscope (FESEM) picture of the closely packed M2 unit cells spanning over an area of 150 μm by 150 μm. The process is optimized to maximize the lift off success rate and minimize the peeling off rate of the highly dense and complex shaped patterns. Figure 2(b) shows the zoomed in picture of the unit cell. Note that, the minimum spacing between the unit cells achieved is 110 nm whereas the minimum cross-coupling distance is found to be 44 nm. The false colored section of figure 2(b) also shows the successful fabrication of the quasi self-symmetric radiators numbered from I to IX. The nanometric details in figure 2(c) reveal the strong presence of corner roundedness of different radii that

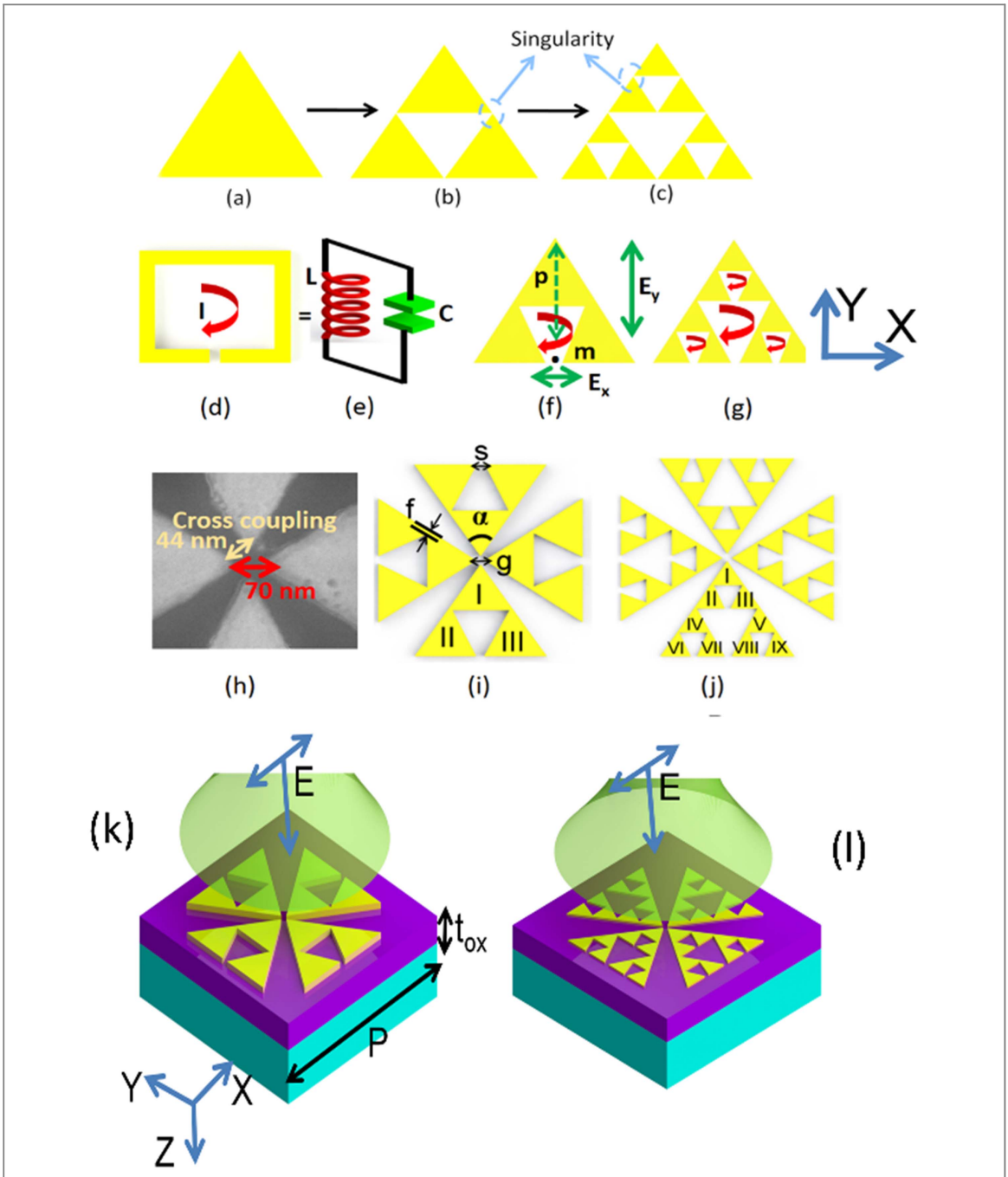

Figure 1. (a) Triangle without any fractal inclusion. (b) Sierpiński fractal layout of order 1 and (c) order 2. The presence of the geometric singularity at the acute corners is indicated. (d) Conventional split-ring with circulating current (I) and its (e) equivalent LC circuit model. (f) Modified Sierpiński triangle of order 1 with a narrow conduction path at the previously indicated singularity zones and a split gap for magnetic excitation; **p** and **m** denote the moments of the dipolar mode and magnetic mode, respectively. (g) Modified Sierpiński triangle of order 2 with a scaled up number of magnetic pathways. (h) Cross-coupling between the vertical and horizontal bow-tie pairs located at a proximity of nanoscale to each other. Cross-coupled configuration derived from the (i) first order fractal layout (j) second order fractal layout. f and s denote the width of the conduction path and split gap, respectively while the roman numbers indicate the self-symmetric radiators of the fractal patterns. (k) 3D schematic of the first order (M1) device. (l) 3D schematic of the second order (M2) device. The gap size g and the vertex angle α are fixed at 100 nm and 60 deg., respectively. The thickness of the oxide layer t_{ox} and the gold patterns are kept constant at 1 μm and 35 nm, respectively. The pitch P is pushed down to 2.77 μm to maximize the near field coupling of the unit cells.

mainly occur due to the backscattering of the e-beam. Such imperfection can cause the spreading of Coulombic charges and yield strong blue-shift of resonance in the far field by increasing the restoring force [25, 26]. In fact, such rounding can occur whenever there is a presence of sharp tip and thus affect the resonance specific charge distribution presented in our discussion on charge density maps. We limit the order within 2 in this work as the growth of the fractal is critically constrained by the fabrication limit. Finally, figures 2(d) and (e) show the M1 unit cell with its radiators and the nanometric details, respectively.

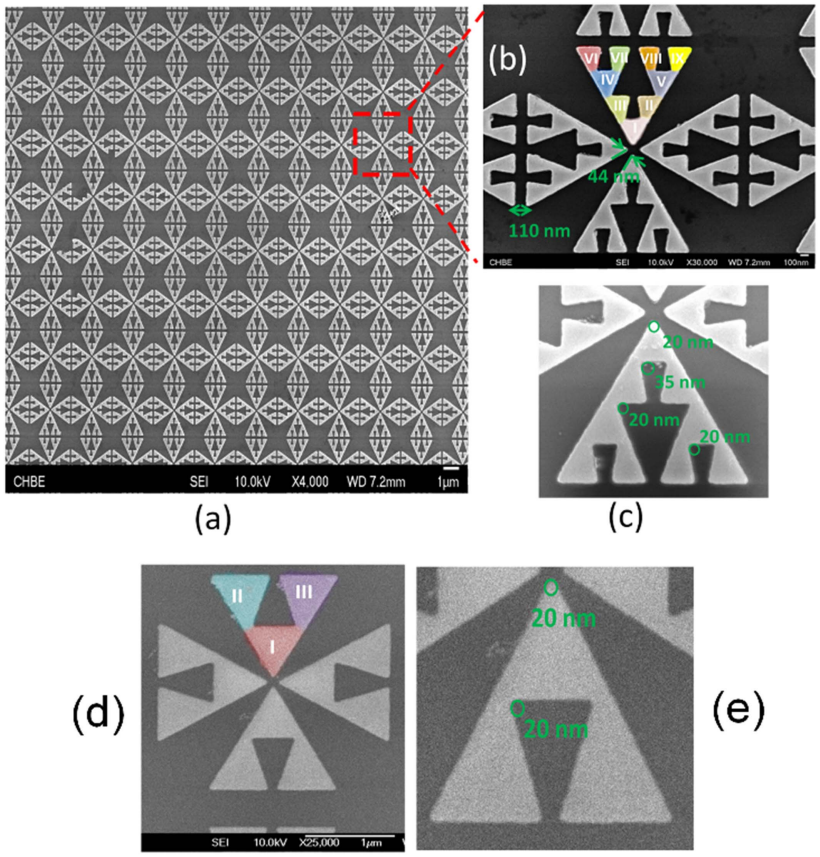

Figure 2. (a) An FESEM image of the highly dense array of the M2 device, (b) zoom-in view and false colored self-symmetric radiators of the M2 unit cell, (c) nanometric roundedness of the corners and tips after fabrication, (d) zoom-in view and false colored image of the self-symmetric radiators of the M1 unit cell, (e) nanometric roundedness of the corners and tips after fabrication.

2.3. Characterization

The normalized transmission and reflection spectra have been obtained by a broadband Agilent Fourier transform infrared (FTIR) spectroscopy system. The area of the aperture is considered to be 100 μm by 100 μm. The reflectance of the devices is normalized with respect to that of a smooth gold surface and transmittance is normalized with respect to the free space transmission of light. The size of the aperture was adjusted carefully to match with the size of each square pattern, therefore eliminating the background reflection. The sampling resolution is varied between 2 cm^{-1} and 8 cm^{-1} depending on the purpose. No polarizer has been used in order to perform polarization independent measurement. The mirror repetition rate is fixed at 40 kHz and the number of scans is maintained to be 64. A three dimensional finite difference time difference solver has been deployed to simulate the reflection and transmission spectrum under x-polarized light. The near field transmittance/reflectance has been captured by a transmission/reflection monitor placed 15 μm away from the metal patterns. The simulation region has been terminated by periodic boundary conditions along the x and y direction and perfectly matched layer along the z direction. A spatial resolution of dx $=$ 1 nm, dy $=$ 1 nm and dz $=$ 1 nm is chosen for accurate calculation. Optical properties of gold have been extracted from Palik and the refractive indices of Si and SiO_2 have been fixed at 3.5 and 1.45, respectively. In the experiment, an unpolarized light source is incident out-of-plane within a cone of angles ranging from 0 deg. to 20 deg. Simulation has been carried out by varying the polarization angle and angle of incidence. No significant dependence of the resonance characteristics on the polarization angle and angle of incidence is observed in simulation. Thereby, the detailed study of the parameter effect has been carried out at a single polarization angle and angle of incidence. Also, the roundedness of the nanostructure corners is observed due to the scattering of electron beams, which can possibly lead to blue-shift of resonances. Due to the complexity of the nanostructure, such an effect has not been considered in the present simulation model.

2.4. Physical mechanism and geometric effect

Figure 3(a) shows the experimentally collected reflectance spectra of the M1 device with two distinct peaks: D1′ and D2′. The simulated results presented in figure 3(b) are in agreement with the experimental results except for the pronounced blue-shift in the experiment, which could be a combined outcome of the metal damping in the far field when the near field coupling is potentially strong [27–29] and proximity induced roundedness of the

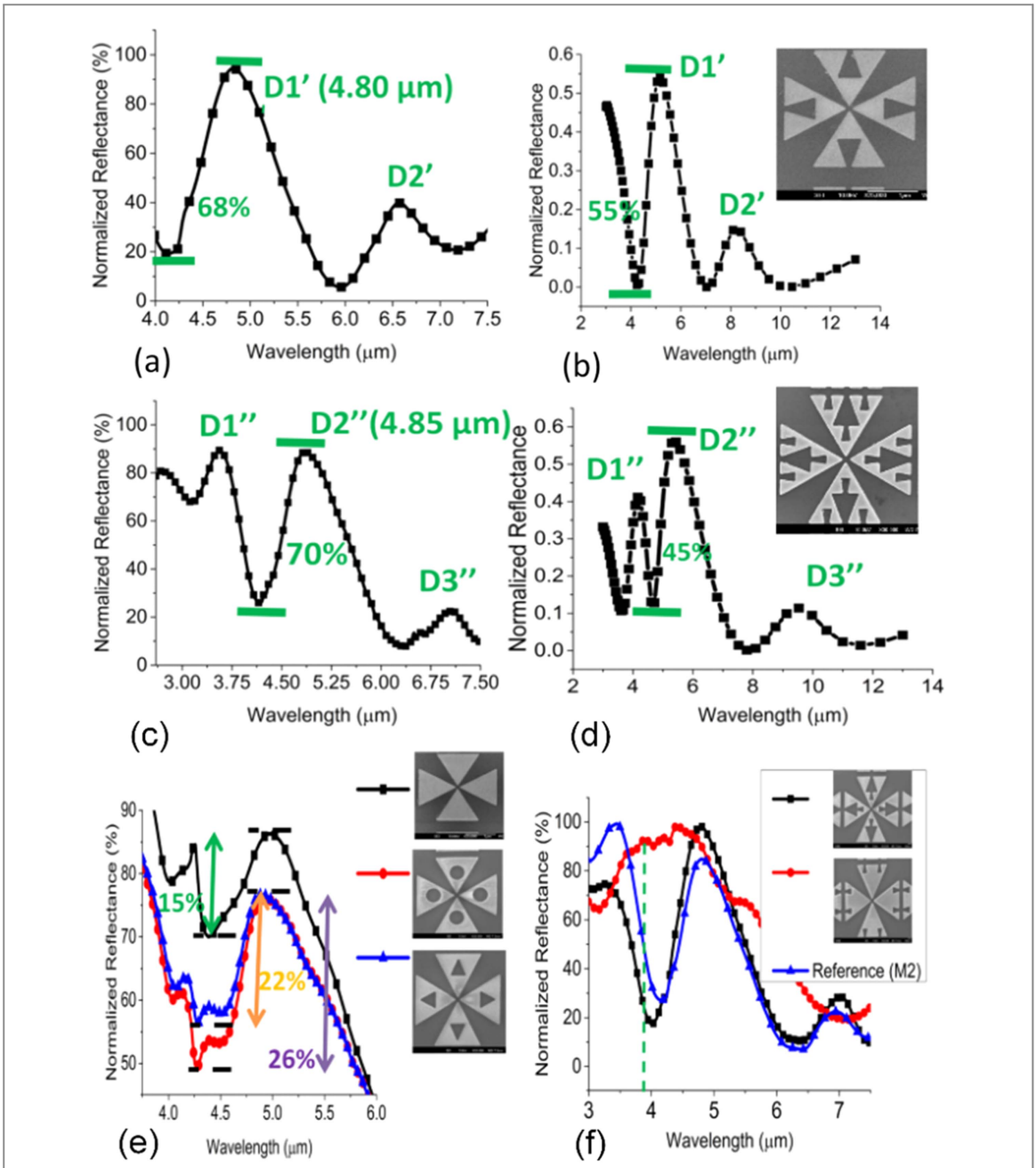

Figure 3. Normalized reflectance of the M1 device (a) experiment (b) simulation, where f and s are kept constant at 70 nm and 100 nm, respectively. Normalized reflectance of the M2 device (c) experiment (d) simulation. (e) Experimentally observed normalized reflectance profile of the three cases of bow-tie configuration. The minimum spacing between an inclusion and the outer edge is kept constant at 70 nm. (f) Spatial origin and mutual coupling of the resonances in the M2 device. The dashed green line indicates the presence of the resonance from the bow-tie triangle bases under unpolarized light.

fabricated patterns. The role of metal damping at mid-IR is verified by simulating the structures while replacing the real metal by perfect electric conductor (PEC). The resonant E-fields in the M1 device are shown in figures 4(b) and (c) at D1′ and D2′ mode, respectively. From figure 4(a), it is evident that D1′ is a dipolar mode with unique field distribution. On the contrary, D2′ is an electrically excited magnetic mode which is analogous to the modes existent in the canonical split-ring architecture and its derivatives [30, 31]. Excitation of such magnetic resonance has both fundamental and technological value for purposes such as understanding the dynamics of weak magnetic emission or devising optical detectors for magnetic field [32–39]. More importantly, excitation of magnetic mode is critical for extending the range of operating wavelength into the far-IR spectrum when the footprint is an important performance metric. Figure 3(c) shows the experimentally observed locations of the three distinct peaks: D1″, D2″ and D3″ of the M2 device which are also in agreement with the simulated peaks in figure 3(d). This time the dipolar mode (D2″) shifts from 4.80 μm to 4.85 μm. Such red-shift as the fractalization order increases is routinely observed in our simulation and experiment (figure 4, supplementary information is available online at stacks.iop.org/NANOF/2/025005/mmedia). Besides, we

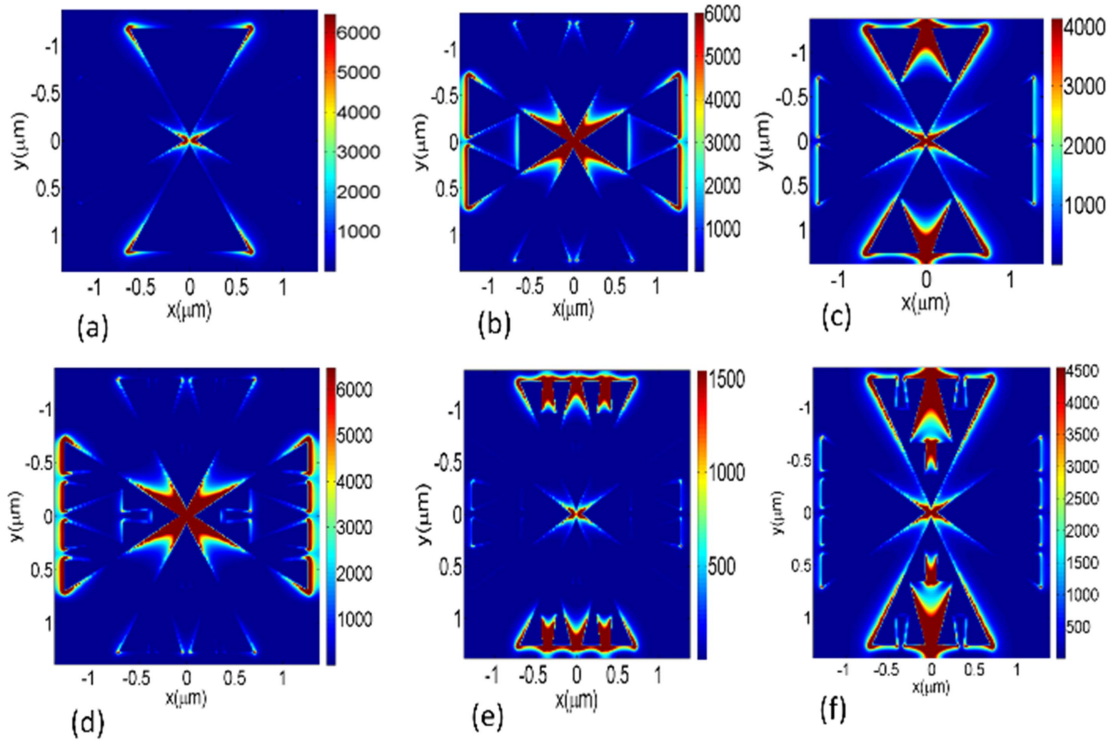

Figure 4. E- field intensity distributions on the xy plane: (a) conventional structure at dipolar resonance; (b) M1 at D1′ (dipolar) resonance; (c) M1 at D2′ (magnetic) resonance; (d) M2 at D1″ (magnetic) resonance; (e) M2 at D2″ (dipolar) resonance; (f) M2 at D3″ (magnetic) resonance.

observe a new peak D1″ on the left side of the dipolar peak. The previously discussed magnetic peak on the right side of the dipolar peak is also shifted further (D3″). Figures 4(d), (e) and (f) show the E-field distribution of the higher order device (M2) at the three distinct resonances. One can comprehend from the E-field distribution that, D1″ is the new magnetic mode encompassing the smaller cavities obtained in the M2 device. The dipolar mode D2″ apparently possesses a similar kind of E-field distribution whereas the magnetic mode D3″ is resonate within a larger cavity surrounded by all the radiators marked in figure 2. Consequently, the D3″ mode is more prone to fabrication imperfection as illustrated in figures 2(c) and (e) than the D1″ mode in the M1 device and maintains larger spatial overlap with the surroundings.

It is notable that such a mechanism of exciting magnetic resonances in a 'single layer' bow-tie nanostructure with the help of fractalization has not been reported before [40]. Additionally, we demonstrate later in the text that these magnetic modes are strongly coupled to the dipolar modes due to their proximity in nanoscale and thus can be regarded as a new avenue for plasmonic sensing with strong feedback. Besides the mid-IR optical magnetism, we also report a dramatic enhancement of dipolar resonance contrast when compared to the conventional bow-tie geometry as shown in figure 3(e), which can improve the signal to noise ratio in microfluidic detection significantly [41]. We identify two concurrent mechanisms of such enhancement from our experiments. Firstly, the damping effect of plasmons in noble metal, e.g. Au at mid-IR on the quality factor of the device can be partially suppressed by reducing the area of metal regions [42]. The proposed idea of fractalization and including voids within the unit cell thus can help to improve the resonance contrast. Secondly, we propose that, the resonance contrast can be improved further if all the radiators augment the polarization current density (J) coherently and increase the dipolar moment (p) according to the following equation [43, 44],

$$\mathbf{p} = -\frac{1}{i\omega}\int_V \mathbf{J}(\mathbf{r})\,\mathrm{d}V \tag{1}$$

where V is the volume of integration. To verify our proposition, we consider two additional cases: bow-tie nanostructure with (i) circular inclusion of equal area and (ii) triangular inclusion without the split gap and present the reflectance spectra in figure 3(e). It can be observed that, resonance contrast can be increased from 15% to 26% as the voids are introduced. Such minor improvement is mainly attributed to the reduction of the conduction loss inherently present in the metal film. In a conventional bow-tie nanostructure, the current profile strongly spans over the metallic region and thus causes the deterioration of quality factor (figure S1, supplementary information). On the other hand, the resonance contrasts observed in figure 3(e) are at least three times less than the resonance contrast in figures 3(a) and (c). Due to the increased lightning rod effect, the

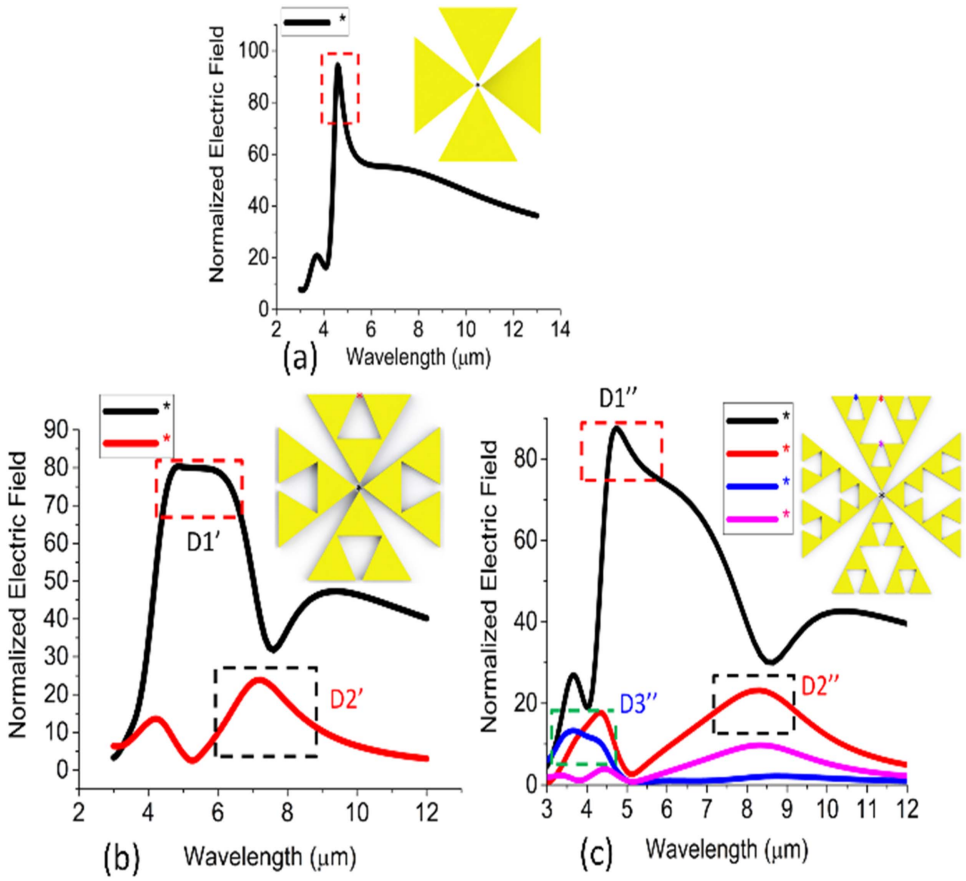

Figure 5. Normalized E-field variation with wavelength at the defined 'hotspots': (a) conventional bow-tie structure; (b) M1 structure; (c) M2 structure. The excitation polarization is along the horizontal direction.

magnitude of J in the M1 and M2 devices becomes 6.5 times and 6 times larger than in a conventional bow-tie, respectively (figures S2 and S3, supplementary information) and thus appends the dipolar moment. Although, it is expected that, the overall moment from the M2 device will be larger since there are three additional pairs of current density (J) 'hotspot' with varying intensities in each of the host triangle. Yet, we find that, the dipolar resonance (D2″) contrast in M2 can be slightly lower than in M1 (figure S4, supplementary information) due to the onset of D1″ nearby D2″ and thus contrasts with the intuition. Another phenomenological outcome of the fractalization is the effective increase of antenna length, i.e. lowering of the restoring force between the opposite charges as highlighted in the discussion on the charge density map. Essentially, the dipolar resonance in M1 and M2 is found to be red-shifted both in experiment and simulation compared to the conventional structure [44]. The proposed idea of split gap and surface current engineering at the acute corners can, therefore, strongly activate the conducting coupling between the self-symmetric radiators and boost the dipolar resonance strength in the mid-IR spectrum. It also provides a unique mechanism to achieve optical magnetism at mid-IR on a highly scalable platform and the corresponding magnetic moment, **m** is defined as below [43],

$$\mathbf{m} = \frac{1}{2}\int_V \mathbf{r} \times \mathbf{J}(\mathrm{r})\mathrm{dV} \tag{2}$$

where V is the volume of integration and r denotes the vecorial polar coordinate. Here, the x-component of the circulation current (J) is providing the necessary moment along the z direction (m_z) at the magnetic resonances. Next, we decompose the M2 structure in figure 3(f) to understand the spatial origin and mutual coupling of the individual resonances. With respect to the reference structure (M2), significant changes of resonance intensity and spectral position are observed at the D1″, D2″ and D3″ modes meaning strong coupling among the resonances. For example, D1″ mode is not distinguishable as the central cavity in the M2 structure is removed. The simulation results in figure S7 of the supplementary information further confirm such an observation. Thus, the results in figure 3(f) suggest the need for strong coupling among the different voids of the M2 structure for strong excitation of the D1″, D2″ and D3″ modes. Finally, using near field simulation, we demonstrate such mutual coupling in a 'single layer' device in figure 5, which we regard as a powerful feedback tool for plasmonic sensing of localized perturbation. We put the electric field monitors in different electric field 'hotspots' at the mid plane of the metal patterns as shown in figure 5. The total number of 'hotspots' can be as high as 17 in the

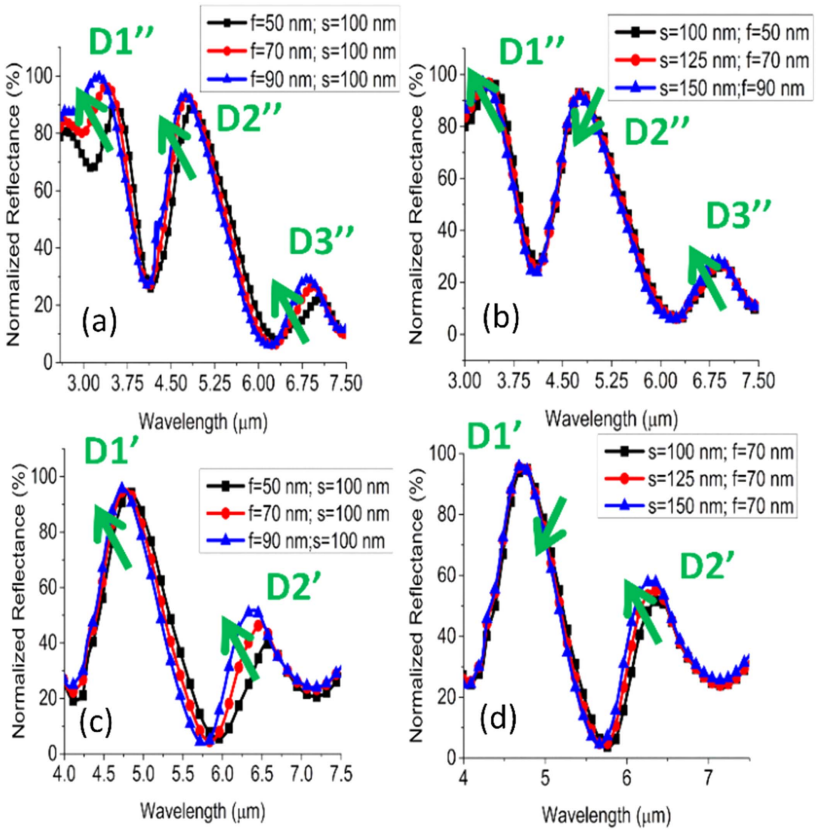

Figure 6. Effect of (a) f and (b) s on the M2 device. Effect of (c) f and (d) s on the M1 device.

fractalized devices (M2) as opposed to only 1 in the conventional structure. Note that, due to the strong diffractive coupling in the highly dense array of nanostructures, we observe the asymmetric and narrow profile of electric field magnitude in figure 5(a) in the case of the conventional structure which again declines rapidly and becomes flatter on the red side of the peak. The same profile becomes relatively broader in the case of the M1 and M2 devices, as shown in figures 5(b) and (c), while maintaining the comparable electric field magnitude. The broadening of the electric field spectrum implies strong charge localization at the tips of the horizontal triangles over a certain bandwidth.

Thus, the culminated moment in the dipolar regimes (D1′ and D2″) is larger than in the conventional structure according to Aizpurua *et al* [44] and validates the improved resonance contrasts as discussed previously. Interestingly, the electric field magnitudes in the 'hotspots' of the vertical triangle resonantly drops in figures 5(b) and (c) at the D1′ and D2″ regimes. The vertical pair is providing the excitation path of magnetic modes and at the same time, is strongly cross-coupled to the horizontal pair. Thus, a peak in the dipolar 'hotspot' appears as a dip in the magnetic 'hotspots' as the amount of induced charge is significantly affected. Similarly, in the magnetic regimes (D2′, D1″ and D2″), we find that the E-field magnitude at the dipolar 'hotspot' resonantly drops. In other words, the voids in the fractal patterns are conductively coupled to each other and can be utilized as a powerful feedback tool for mid-IR sensing. Later, we demonstrate how such effect can be useful for optical monitoring of the chemical dewetting process of monolayer polymer substance.

The following section is devoted to the discussion on capacitive and inductive tuning of resonances of the proposed designs for narrow band surface enhanced infrared absorption spectroscopy [45]. Figure 6 shows the overall picture of the M1 and M2 resonances as the two parameters: f and s are varied with nanometer precision. Here, the parameter f causes the inductive tuning by directly acting upon the conductive coupling of the sub-wavelength features; triangular radiators in our case. It can be observed from figures 6(a) and (c) that, as f is decreased, all the resonances red-shift. The shift of magnetic resonances is found to be more pronounced than the shift of dipolar resonance. The similarity between M1 and M2 devices observed, suggests the existence of a well-constructed set of design rules for the fractal derived patterns. Tuning of both the properties, resonance wavelength and intensity, can be roughly interpreted using circuit theory. The resonance wavelength at dipolar and magnetic mode can be approximated as, $\lambda \infty \sqrt{LC}$ where L and C are the bulk inductance and capacitance of the structure, respectively [46, 47]. The resonance intensity enhancement is related to the enhancement of

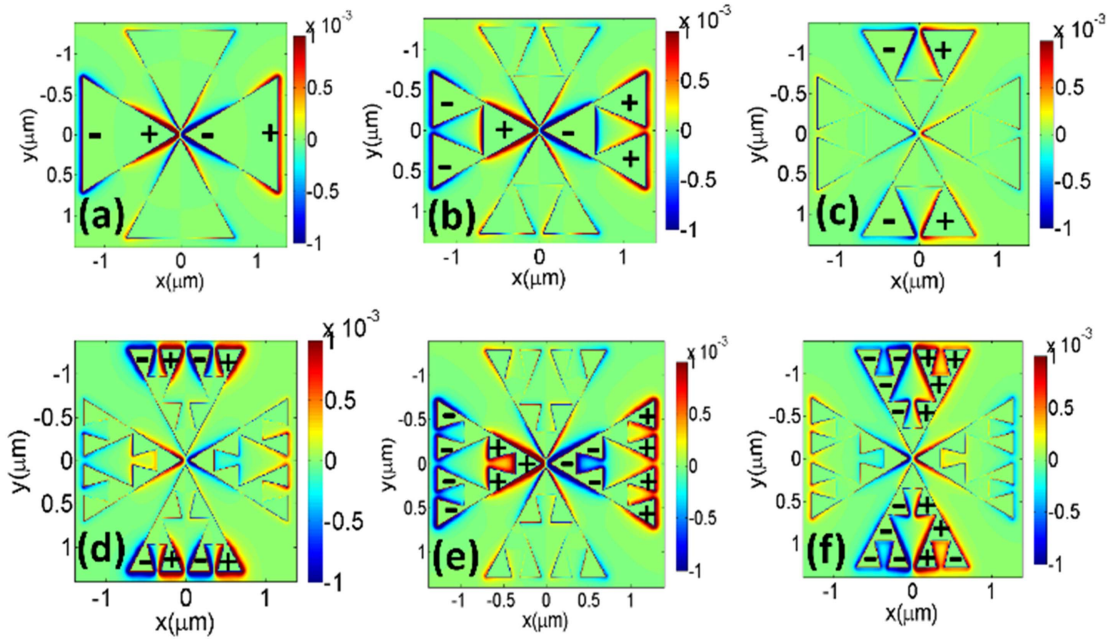

Figure 7. Charge density map: (a) dipolar resonance in a conventional bow-tie, (b) D1′resonance, (c) D2′ resonance, (d) D1″ resonance, (e) D2″ resonance, (f) D3″ resonance.

quality factor (Q) which can be expressed as $2\pi cL/\lambda R$ where R can quantify the radiation damping of the metallic nanostructures at mid-IR. In case of the magnetic mode with circulating displacement current, decreasing f will increase the effective inductance as the area of the loop is increased.

On the contrary, for the dipolar mode, decreasing f can increase the magnitude of current density J and increase the effective inductance of the dipolar antenna. Both of these mechanisms can increase the resonance wavelength according to the equation described previously. It is reasonable to argue that, at higher resonance wavelength, the damping resistance (R) of the metal will be higher. Hence, despite this, there is an increase of L in the numerator of the quality factor expression, ultimately the overall value of Q is found to decline, that also involves the decrease of resonance intensity. Conversely, the influence of s on resonant properties is found to be much weaker in figures 6(b) and (d) than f. This is so, because f can strongly modulate the conductive coupling amongst all the radiators whereas s mainly introduces the capacitive effect at the gaps. As s is increased, the overall inductance under dipolar mode can be assumed to be slightly decreased whereas the gap capacitance is strongly scaled down according to $C\infty 1/s$ at mid-IR.

In what follows, both dipolar and magnetic resonance blue-shift, of which the magnetic mode is more dominant. The negligible drop in dipolar resonance intensity is possibly due to the decrease of overall inductance as s is increased. We present the detailed simulation study of M2 in which a strong agreement with the experiment is observed as the parameters are varied (figures S6 and S7, supplementary information). The charge density maps in figure 7 reveal a rather complex picture of the underlying physics of geometric tuning [48–51]. It can be observed from figures 7(a), (b) and (e) that fractalization can strongly redistribute the dipolar charge accumulation and manipulate the net restoring force of the structure. Strong repulsive force can be generated between the like charges within the radiators in addition to the attractive force between the opposite charges. Consequently, the restoring force may reduce rendering a red-shift in the spectrum. Magnetic mode charge distributions in figures 7(c), (d) and (f) indicate that, both attractive and repulsive force can be generated within a cavity resonant at a particular wavelength. The interplay between these two forces can be strongly engineered by the two parameters: f and s. Furthermore, the induced charge at the tips of the non-resonant pair of triangles is clearly observed in figure 7 implying the strong presence of cross-coupling.

In table 1, a quantitative comparison between M1 and M2 devices in terms of change of resonance intensity and location as the parameters are varied is presented.

The data in table 1 show that M2 resonance shifts per nm variation are dominant over M1 resonance shifts irrespective of the nature of the mode, except for D3″ when the variable is s. Similarly, the intensity change per nm in M2 is higher than in M1 for the dipolar mode. However, no conclusive arguments could be reached for the magnetic modes (D3″ and D1′) due to the factor such as mismatch of M1 and M2 resonance wavelength.

Table 1. Role of f and s on geometric tuning of resonances in M1 (top) and M2 (bottom) device.

Resonance	f		s	
	$\Delta\lambda$ (nm) per nm	ΔI (%) per nm	$\Delta\lambda$ (nm) per nm	ΔI (%) per nm
D1′	2.475	0.0288	0.48	0.0126
D2′	3.7	0.295	1.98	0.1246
Resonance	f		s	
	$\Delta\lambda$ (nm) per nm	ΔI (%) per nm	$\Delta\lambda$ (nm) per nm	ΔI (%) per nm
D1″	7.4	0.263	2.34	0.0058
D2″	3.1	0.119	0.625	0.0235
D3″	6	0.167	1.98	0.0314

3. Functional study of molecular fingerprints in the non-resonant regime mediated by cross-coupling

3.1. Strong coupling to the molecular fingerprints in the non-resonant regime

We deploy the fractal engineered voids for the non-resonant detection of molecular fingerprint of ultra-thin polymer layer. Such label–free detection of chemical specific vibrational modes of monolayer at mid-IR is a versatile screening technology in proteomics. Unlike the previous resonant approach, we observe the presence of the weak optical signature in the non-resonant regime of the structure implying its broadband characteristics for the universal detection of a myriad of chemicals. Firstly, we demonstrate our modified idea of fractalization as a systematic approach to increase the spatial overlap for a strong excitation of a coupled, hybridized resonance. We choose the phonon vibrational mode of poly(methyl methacrylate) (PMMA) carbonyl bond (C=O) located at 5.79 μm for demonstration. The functional devices are obtained by spin coating the patterns with 110 nm thick PMMA film. Figure 8(a) shows the steps and side wall profiles after the coating. The uniformity of the coating can be estimated by the small deviation of phase angles (16.3 deg.) in the phase map of figure 8(b). The dielectric constant and the vibrational transition of PMMA at mid-IR have been incorporated into the simulation by a Lorentzian model [52]. The coupled mode resonance can be studied by the following sets of equations derived from the coupled mode theory [53, 54],

$$\Delta\omega = -\frac{1}{2}\omega\frac{\int_0^t E.\Delta\epsilon.EdV}{\int_0^\infty |E|^2 dV} \tag{3}$$

$$\omega'_M = \frac{\omega_M + \omega_C}{2} + \left(\frac{\omega_M - \omega_C}{2}\right)\left[1 + \frac{\nu}{\left(\frac{\omega_M - \omega_C}{2}\right)^2}\right]^{\frac{1}{2}} \tag{4}$$

$$\nu = \gamma_A\gamma_C + |\kappa_{AC}|^2. \tag{5}$$

Here, E, $\Delta\omega$, $\Delta\epsilon$, ω_M, ω_C, ω'_M, ν, γ_A, γ_C and κ_{AC} are the time averaged electric field, frequency shift from the perturbation theory, change of dielectric constant, resonance frequency of the uncoupled patterns, resonance frequency of the uncoupled vibrational mode, resonance frequency of the coupled patterns, overall coupling coefficient, loss rate of pattern resonance, loss rate of molecular resonance and the mutual coupling strength between the resonant mode and vibrational mode, respectively. Figure 8(c)–(h) shows the relative improvement of quality factor of the resonance dip as the fractal voids are included in the solid pattern. Considering the asymmetry of the hybridized resonance dip, we define two different contrasts: I_L and I_R on the blue side and the red side of the dip, respectively. It can be observed that, the average contrasts $(I_L + I_R)/2$ of the M1 and M2 device in figures 8(c) and (d) clearly outperform the contrast of the cases shown in figures 8(f)–(h). In fact, the M2 device shows larger contrast than the M1 device and the major contribution stems from the central cavity of the M2 device, as it is inferred from figure 8(e). The results clearly interlink the improvement of the contrast with the systematically increased overlap of plasmonic mode with the phonon mode of PMMA thin film. One quantitative estimation of the increased spatial overlap is the resonance shift as indicated in figures 8(c) and (d). The values of $\Delta1''$, $\Delta2''$ and $\Delta3''$ are found to be 800 nm, 850 nm and 1100 nm, respectively as opposed to the values of $\Delta1'$ and $\Delta2'$, which are found to be 500 nm and 909 nm, respectively. Clearly, the sensitivity of the M2 structure dominates over M1 for the like modes.

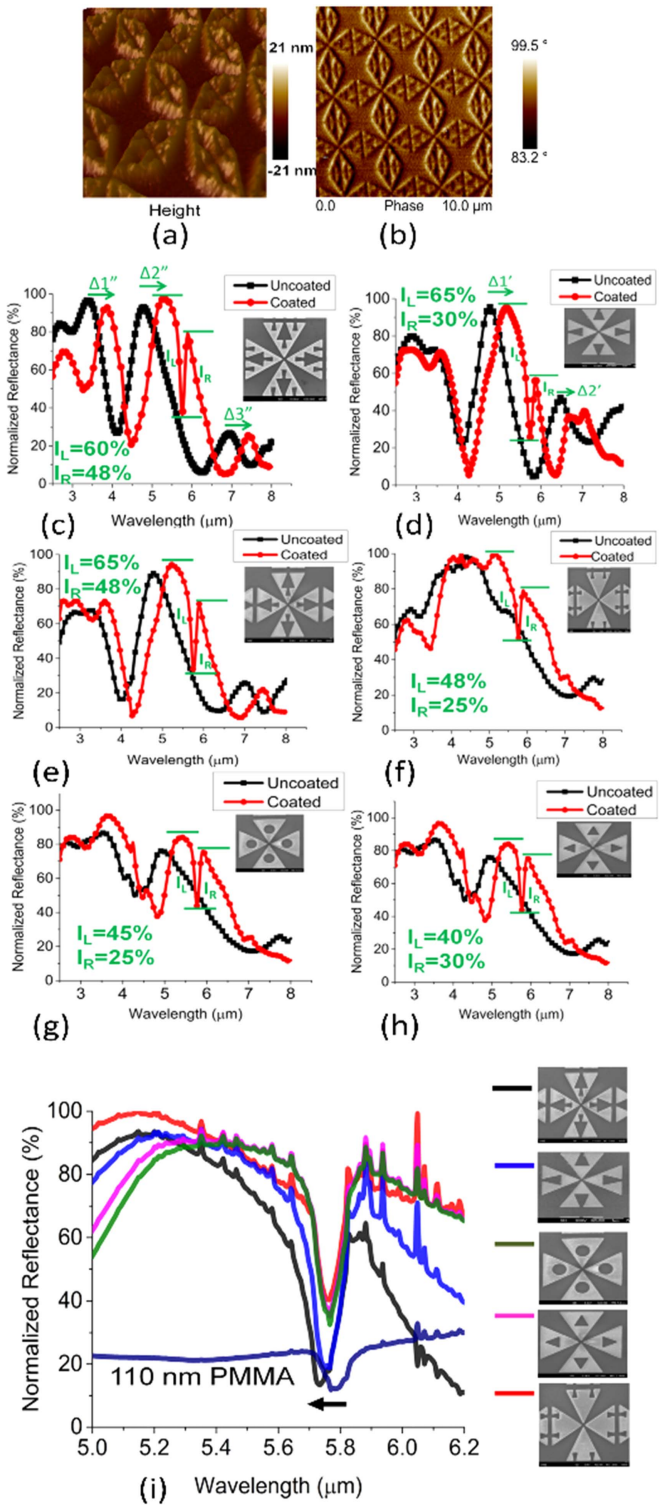

Figure 8. AFM (a) height profile and (b) phase image of the spin coated M2 device. High resolution scanning (2 cm^{-1}) of the variation of resonance coupling at hybridized mode for different geometries. Intensity change of the overall reflectance spectrum as a function of temperature for the cases (c)–(h). (i) Zoomed in change of the reflectance dip intensity at the hybridized mode as the temperature is varied.

We further conduct a high resolution scanning of the hybridized mode in figure 8(i) for different cases. The relative shift between the thin film dip and the coupled dip becomes the highest for the case with the largest cavity derived from second order iteration. According to equation (4), the blue-shift of the coupled dip is a strong function of the overall coupling coefficient ν which, in turn depends on κ_{AC} according to equation (5). Here, we propose that, κ_{AC} can be enhanced through a systematic engineering of spatial overlap aided by the fractal voids. Please note that, under all circumstances, the hybridized reflectance dip is located far from the

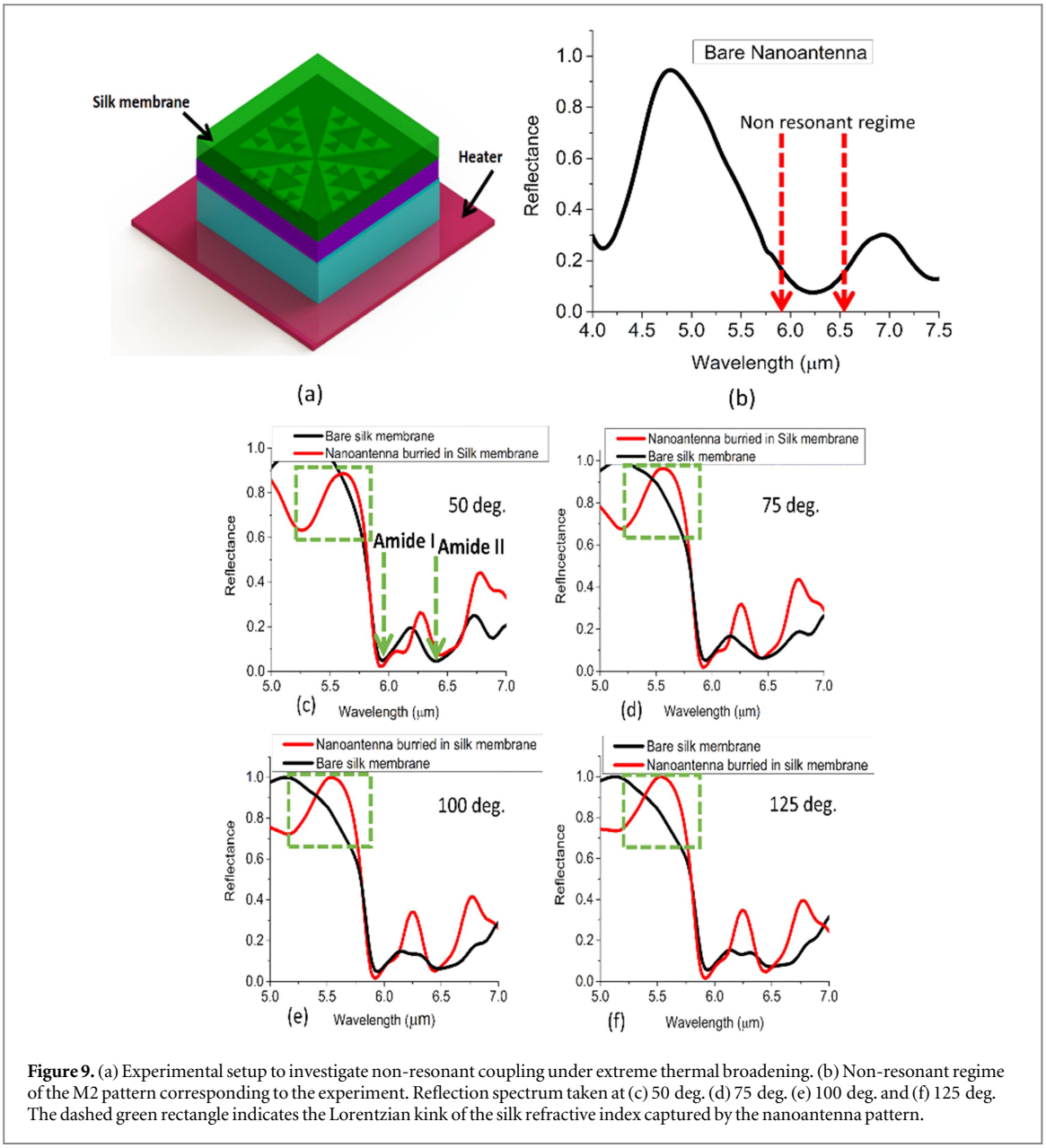

Figure 9. (a) Experimental setup to investigate non-resonant coupling under extreme thermal broadening. (b) Non-resonant regime of the M2 pattern corresponding to the experiment. Reflection spectrum taken at (c) 50 deg. (d) 75 deg. (e) 100 deg. and (f) 125 deg. The dashed green rectangle indicates the Lorentzian kink of the silk refractive index captured by the nanoantenna pattern.

dipolar peak of the patterns. Thus, we confirm the non-resonant detection of PMMA vibrational mode using densely packed nanostructures with broadband light–matter interaction. Under non-resonant approximation, such broadband interaction can be expressed as a function of distributed electric field enhancement ($|E|^2$) originating due to the lightning rod effect as below [55],

$$A \infty \left| \frac{\partial \mu}{\partial Q} \right| |E|^2 \tag{6}$$

Here, μ, Q and E are the dipolar moment, vibrational coordinate and the electric field enhancement, respectively, and A denotes the absorbance of the molecular mode determining the intensity of the reflection dip. To support our argument, we conduct another set of experiments on silk membrane (500 nm) in a different non-resonant regime and under extreme thermal broadening [56]. The setup and the non-resonant regime are shown in figures 9(a) and (b), respectively. It is observed that the vibrational bonds of bare silk membrane can undergo a pronounced broadening due to a moderate increase of temperature. In other words, the dipole moments of the bonds are significantly affected as the temperature is increased. However, almost no change in the spectrum is observed when the silk membrane is spin cast on the nanoantenna pattern. It clearly signifies the dominance of electric field enhancement by the fractal pattern (M2) in equation (6) over the change of the dipole moment at elevated temperature.

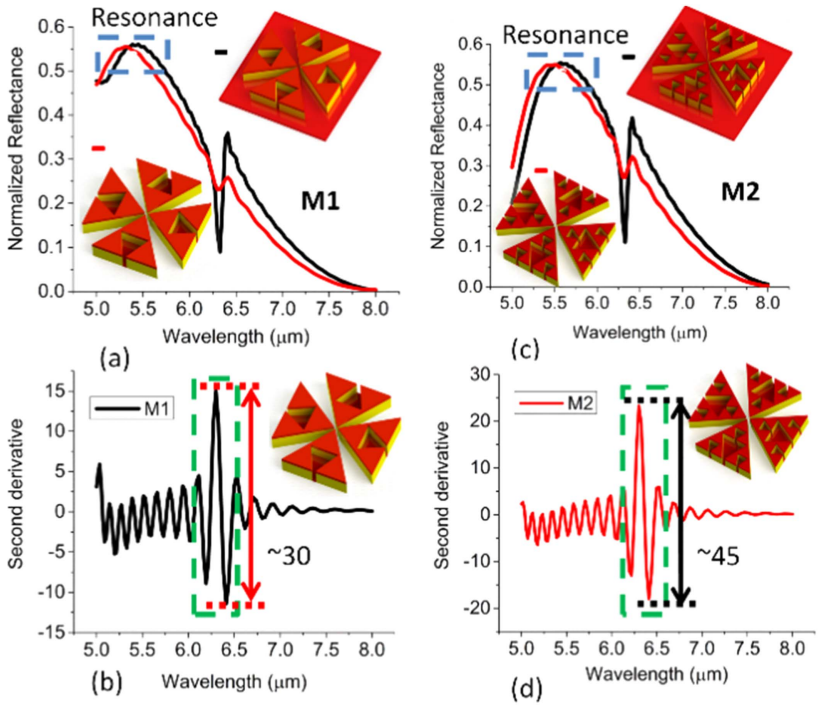

Figure 10. (a) Detection of a molecular fingerprint from PMMA ultra-thin film (5 nm) in the M1 device. (b) Second order derivative of the reflectance change in the M1 device. (c) Detection by the M2 device. (d) Second order derivative of the reflectance change in the M2 device. The blue dashed rectangle implies the nearby resonance. Thus, the detection is performed in the non-resonant regime of the devices. The green dashed rectangles imply the change of the second order derivative corresponding to the vibrational feature in the spectra.

3.2. Detection of monolayer in the non-resonant regime and functional study of its solid state dewetting

We then focus on the ultra-thin coating (~5 nm) of the sample. First, we verify the role of the fractalized cavities of the nanopatterns on enhancing the absorption signal of the uniform monolayer using simulation. We consider the two cases in simulation as shown in figure 10 for each of the devices. The ideal cases of the patterns partially buried by the 5 nm thin film show a strong presence of the vibrational mode in the non-resonant regime of the spectra in figures 10(a) and (c) which we attribute to the interaction between the thin film absorption and 'hotspots' located at the outer edges of the nanostructures. The second derivatives of the reflectance spectra (red solid line) of figures 10(a) and (c) are also plotted in figures 10(b) and (d), which is a powerful tool to quantify the minute change in the spectrum. Clearly, the response is relatively weak when the interaction is only limited between the inner edges of the nanostructures and thin film. Since the M2 device has higher spatial overlap, i.e. higher interaction with the thin film, higher sensitivity is observed as expected. In our experiment, the thin PMMA coating is obtained by spinning diluted 5% PMMA solution in anisole at a speed of 6000 rpm. The AFM analysis before and after the functionalization clearly shows a height difference of ~5 nm indicating the presence of the ultra-thin layer (figure S8, supplementary information).

The unique feature of bow-tie geometry is the presence of the sharp tip where a strong localization of charge density can be achieved. Such a property allows us to exploit a less studied phenomenon, namely cross-coupling, by placing two pairs of bow-ties: (i) transverse/horizontal (along the x-axis) and (ii) longitudinal/vertical (along the y-axis) within a proximity of nanometer scale with exotic functionalities under arbitrary polarization [57]. Here, we propose the idea of merging magnetic and dipolar mode on a bow-tie platform with the help of fractalization and forming a strongly interacting unit cell. The minimum cross-coupling distance we can routinely obtain is 44 nm as shown in figure 2(b). We suggest that bow-tie configuration will be particularly suitable for cross-coupling mediated sensing due to the ease of achieving nanometric proximity of the tips. In this context, it is necessary to highlight that we observe a strong blue-shift of dipolar resonance in simulation occurring along the transverse pair (horizontal pair along the x-axis) when the longitudinal pair (vertical pair along the y-axis) are removed. Such a shift is associated with the modification of net restoring force due to the induced charges in the longitudinal pair as shown before in figure 7.

Since the unit cells in our case are densely packed with strong near field interaction, the dipolar response can be treated as a summation of the incident field response and the collective response from the ensemble, and can be expressed as below [58],

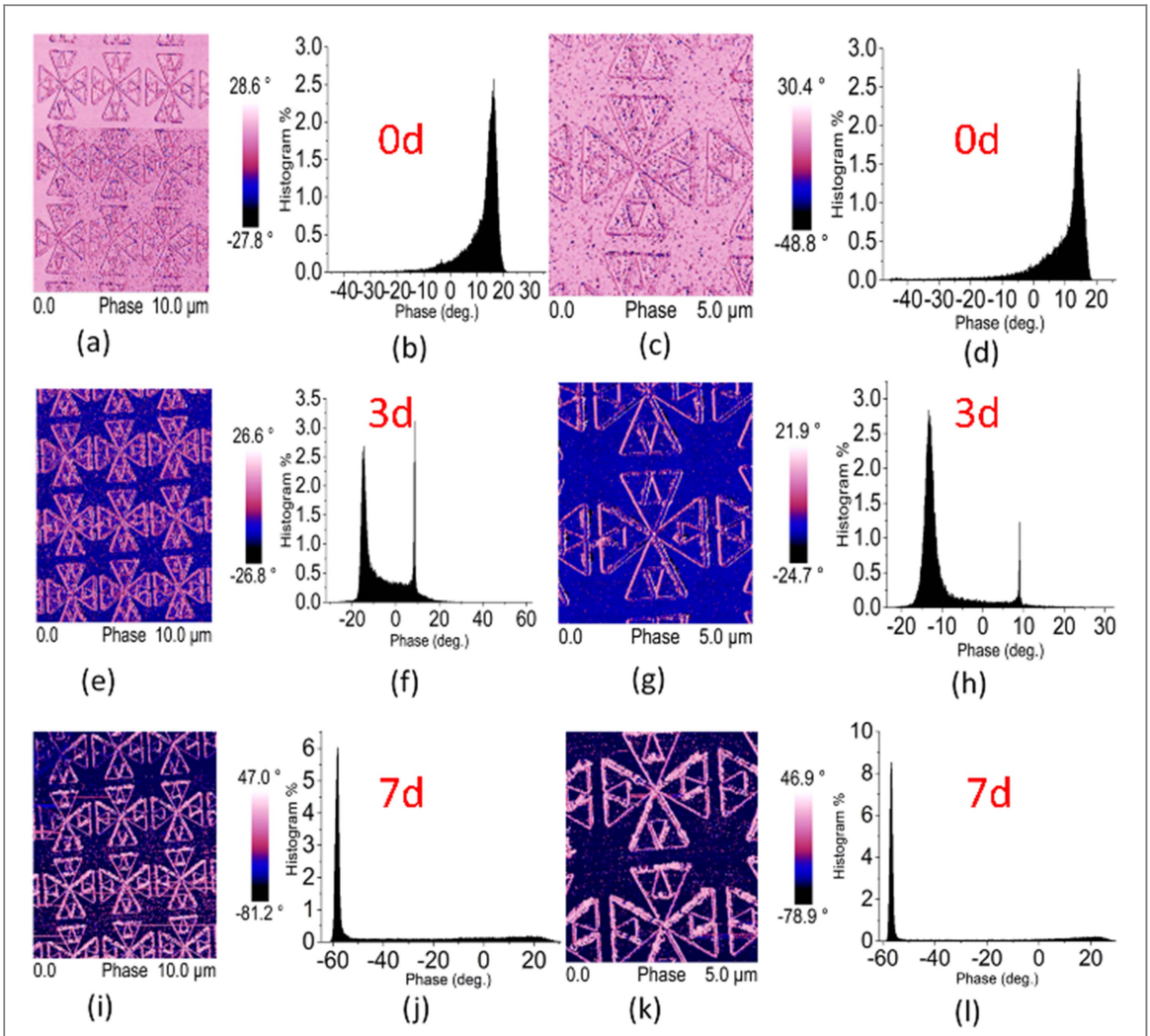

Figure 11. Temporal evolution of the AFM phase profile of the M1 device. (a), (e), (i) Phase map of a 10 μm by 10 μm scanning area after 0d, 3d and 7d, respectively. (b), (f), (j) Phase histogram of the 10 μm by 10 μm scanning area after 0d, 3d and 7d, respectively. (c), (g), (k) Phase map of a 5 μm by 5 μm scanning area after 0d, 3d and 7d, respectively. (d), (h), (l) Phase histogram of the 5 μm by 5 μm scanning area after 0d, 3d and 7d, respectively. The pink regions indicate the presence of PMMA in different states.

$$\mathbf{E}_i = \mathbf{E}_{inc,i} + \sum_{j=1, j\neq i}^{N} e^{ikr_{ij}} \mathbf{C}_{ij} \mathbf{p}_j \tag{7}$$

where i and j are the indices of the unit cells and r_{ij} is the distance between them, C is the dipolar interaction matrix, **p** is the dipolar moment and N is the total number of unit cells. The second term in the above expression implies the sum of the retarded dipolar fields. For a periodic arrangement, the constructive interference of the scattered fields occurs at a particular wavelength when the condition $kr_{ij} = 2\pi m$ is satisfied, where m is an integer. The ideal condition can be partly compromised when the adjacent cells are electromagnetically different and dipolar moments in equation (7) become randomized. One way to do so is to exploit the cross-coupling between the transverse (horizontal) and the longitudinal (vertical) pairs.

To prove this, we carefully study the temporal dependence of the phenomenal dewetting process of the ultra-thin film (~5 nm) spin coated on the M1 and M2 patterns. Chemical dewetting is a spontaneous process when a sufficiently thin polymer film on a surface self-organizes itself into an ensemble of separated objects (figure S9, supplementary information) [59]. The mechanism on a physically/chemically patterned surface is mainly driven by the spatial gradient of the dewettability [60]. As the Volmer-Weber mode of thin film growth suggests, the PMMA film tends to form islands, nucleates, and coalesce with each other [61] and in our case, the fractalized voids significantly influence the dewetting pattern of the film. Thus, the process paves the way to investigate into the light–matter interaction at different 'hotspots' of the fractal nanostructures. We carefully observe the dynamics of the process in our samples over a time duration of 7 days (d) and explore a distinct relationship at different time intervals (0d, 3d and 7d). At every interval, we perform the scanning of the samples using a Bruker AFM over an area of 5 $\times$ 5 μm^2, 10 $\times$ 10 μm^2 and 20 $\times$ 20 μm^2 and collect the height profile and phase profile.

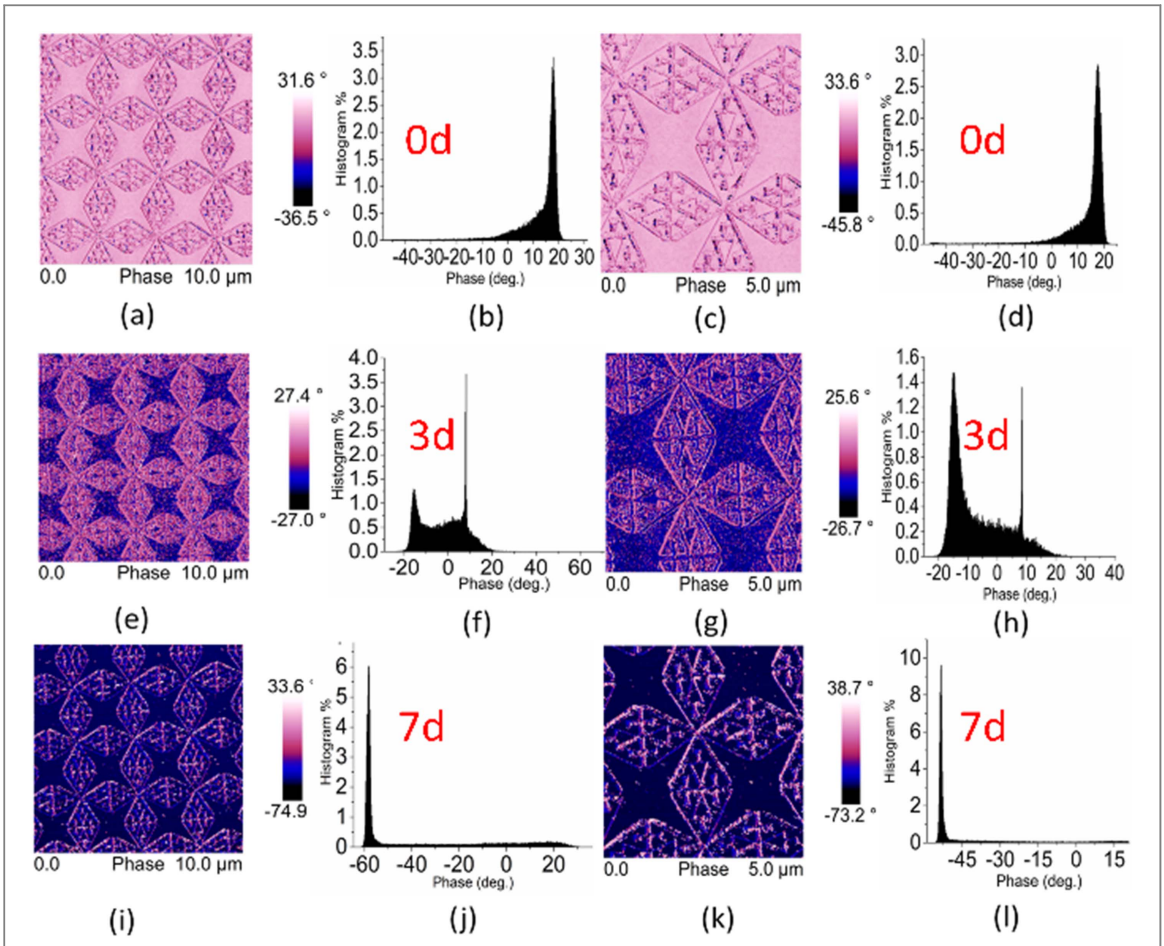

Figure 12. Temporal evolution of the AFM phase profile of the M2 device. (a), (e), (i) Phase map of a 10 μm by 10 μm scanning area after 0d, 3d and 7d, respectively. (b), (f), (j) Phase histogram of the 10 μm by 10 μm scanning area after 0d, 3d and 7d, respectively. (c), (g), (k) Phase map of a 5 μm by 5 μm scanning area after 0d, 3d and 7d, respectively. (d), (h), (l) Phase histogram of the 5 μm by 5 μm scanning area after 0d, 3d and 7d, respectively. The pink regions indicate the presence of PMMA in different states.

We chose AFM phase imaging for the analysis as it is more versatile than the height profiling because of its capability to track the difference of material composition more legibly (figures S10, S11, supplementary information). We extract the phase histogram from the phase profile with the help of the NanoScope Analysis for a qualitative comparison of the intervals. Although only the mappings over 5 $\times$ 5 μm^2 and 10 $\times$ 10 μm^2 areas have been shown in figures 11 and 12 for a better visualization of the phase distribution, the important features of the histograms are found to be almost independent of the size of the scanning area. A close inspection of the time dependent histograms for two different patterns indicates the uniqueness of the PMMA cluster distribution at different intervals. For instance, on the 0d, we can see the thin film homogeneously covering the patterns and substrate (pink region) along with the steps and small ruptures. On the 3d, profound ruptures of the thin film due to the dewetting process are observed. At this stage, it can be assumed that the material composition of the fractal cavities is highly randomized. On the 7d, the continuously evolving dewetting process seems to reach an equilibrium condition and obtains a phase histogram which is entirely different from 0d and 3d. In fact, the PMMA particles are now preferentially located along the edges of the nanopatterns, including the inner edges of the fractalized cavities. To locate the randomly dispersed carbon atoms once the dewetting equilibrium is reached, we carry out further FESEM/EDX mapping of the sample (figures S12, S13, supplementary information). Thus, the dewetting process allows us to investigate into the role of the cavity edges without requiring any functionalization [62]. A close inspection into the phase histograms will also reveal that the morphological state on the 3d is a mixture of the states on the 0d and 7d as the phase angle shifts from positive to negative values.

The time dependent resonance characteristics of M1 and M2 are shown in figures 13(a) and (d), respectively. There are two important features to be highlighted in the spectra: (i) apparently broadened dipolar resonances (D1′ and D2″) and strongly affected magnetic mode (D2′and D3″) on the 3d which revert back to the original shapes on the 7d and (ii) the presence of PMMA fingerprint at 5.79 μm in the M2 spectrum under all three states (0d, 3d, 7d) and in the M1 spectrum only under 3d state. However, second order derivatives of the spectra of figures 13(a) and (d) as plotted in figures 14(a) and (b) clearly indicate ~2 times better detection by the M2

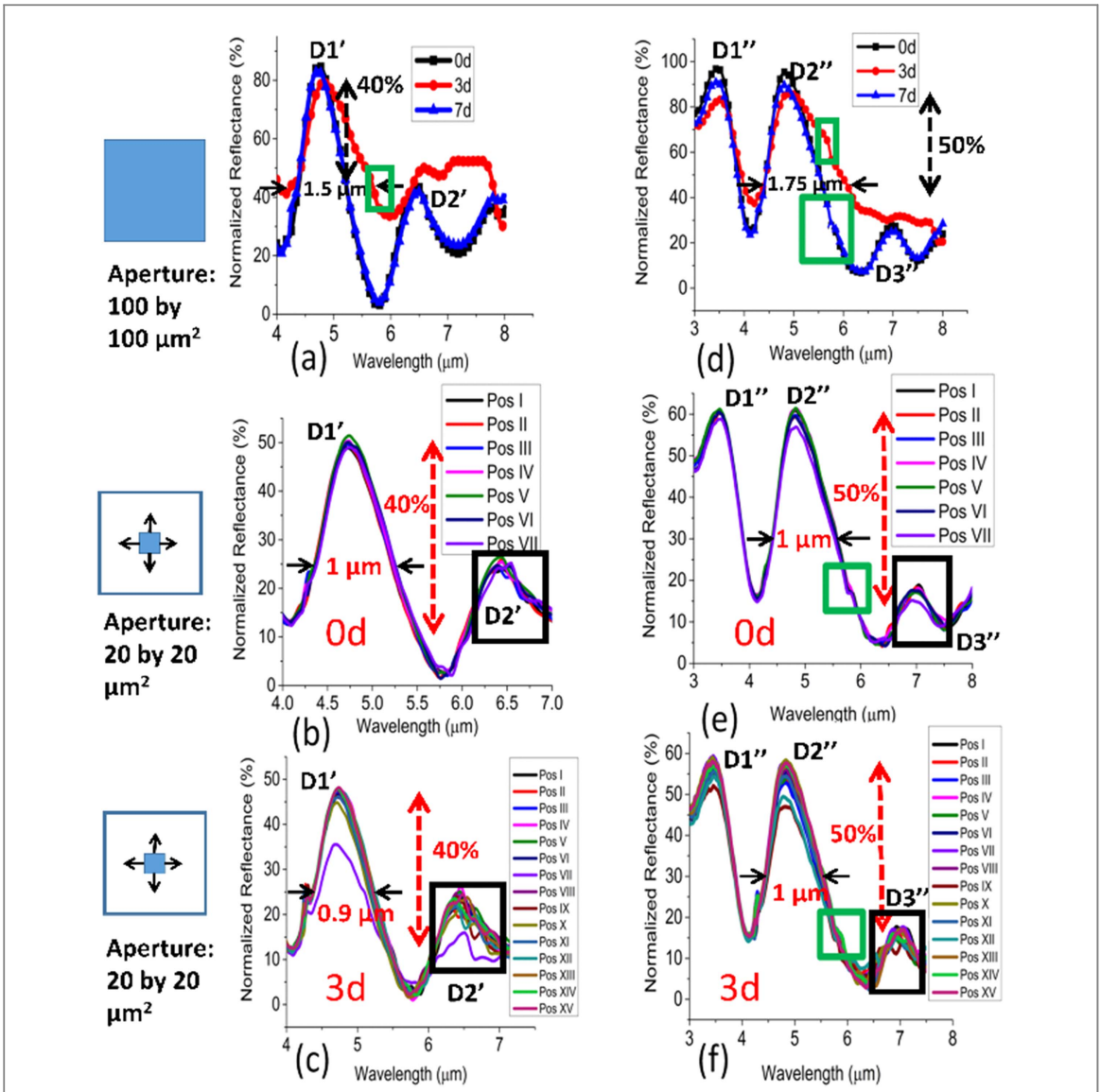

Figure 13. (a) Time dependent resonance broadening in the M1 device. (b) Position dependent M1 resonance profiles on 0d from 20 μm by 20 μm spots. (c) Position dependent M1 resonance profiles on 3d from 20 μm by 20 μm spots. (d) Time dependent resonance broadening in the M2 device. (e) Position dependent M1 resonance profiles on 0d from 20 μm by 20 μm spots. (f) Position dependent M2 resonance profiles on 3d from 20 μm by 20 μm spots. The green solid rectangle indicates the presence of the PMMA fingerprint in the spectrum. The black solid rectangle indicates the magnetic modes (D2′ and D3″) which are more subject to the morphological states. The dashed arrow indicates the relative strength of the asymmetric peak at dipolar mode on the right side.

structure under all states [63]. Moreover, the presence of the fingerprint is only observed in the M2 case in figures 13(e) and (f) when the aperture size is shrunk from 100 by 100 μm^2 to 20 by 20 μm^2. This roughly implies detection of at least 2052 zeptomoles by the discrete, non-complementary nano-architectures in the absence of spoof-plasmons [64]. The explanation for the higher sensitivity of the M2 structure under all three cases lies in the increased electric field interaction within the comparatively larger and distributed nanocavities. The simulation results in figures 14(c), (d), (e), (f) and (g) imply how the distributed near field enhancement is likely to build up in the M2 unit cell under an unpolarized light source. On the contrary, a relatively enhanced detection at the intermediate 3d state is observed in both M1 and M2 cases. We attribute this to the simultaneous contribution of the different 'hotspots' located at the nanogaps and along the edges of the nanostructures which are accessible to the PMMA substance under that particular morphological state.

The cross-coupling mediated feedback is achieved as the dipolar modes (D1′ and D2″) broaden on 3d with the weakening of the magnetic modes (D2′ and D3″). The broadening is associated with a significant decrease in the respective resonance intensity. The magnetic modes are more susceptible to the morphological change along the edges of the nanostructures. In particular, the circulating displacement current ($\mathbf{J} = -\mathrm{i}\omega\mathbf{D}$) flowing through the capacitive gap, produces the necessary out-of-plane magnetic moment of the magnetic modes. As the displacement

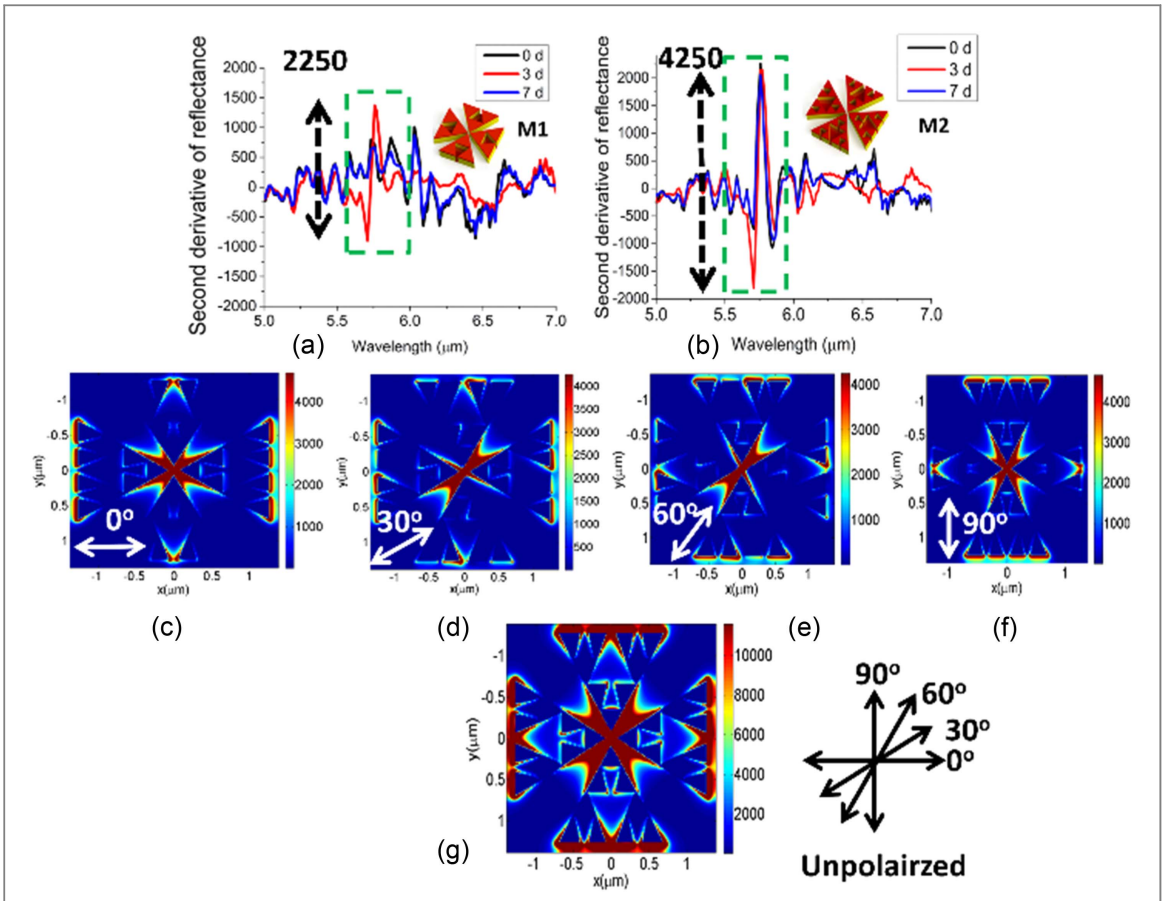

Figure 14. Temporal dependence of second derivative of the reflectance spectra in figures 13(a) and (b) of the reflectance spectra in figures 14(a) and (b): (a) M1 device (b) M2 device. The green dashed rectangle implies the vibrational transition region of the spectra. The dashed arrow indicates the strength of the second derivatives. The simulation wavelength is fixed at 5.79 μm. Electric field intensity distribution in the M2 structure under different polarization (a) 0 deg. (b) 30 deg. (c) 60 deg. (d) 90 deg. (e) distribution obtained by superimposing (a)–(d) .

field is a direct function of the relative permittivity of the gap region, spatial variation of the magnetic mode intensity is reasonable at various morphological states. Note that the FWHM of the dipolar modes in figures 13(b), (c), (e) and (f) are quite identical to each other (~1 μm) on 0d and 3d when the aperture size is reduced to 20 by 20 μm^2, approximately containing **7 by 7** unit cells. However, it increases to 1.5 μm and 1.75 μm for M1 and M2, respectively, on 3d when the aperture size is increased to 100 by 100 μm^2, approximately containing **36 by 36** unit cells. This clearly implies the effect of perturbation of the cross-coupling when the densely spaced nanostructures are collectively excited over a large area. The perturbation of the cross-coupling occurs on the 3d state mainly due to the randomized arrangement of the PMMA substance across the sample. Mathematically, the intermediate 3d state disrupts the diffractive coupling condition as governed by equation (7). Therefore, the spatial variation of the magnetic modes in figures 13(c) and (f) are much more significant when compared to the variation observed in figures 13(b) and (e). Consequently, the magnetic modes are strongly affected when the whole array is collectively excited in figures 13(a) and (d). At the same time, the dipolar modes are collectively broadened due to the spatial variation of cross-coupling under different local environments. The weakening of the magnetic mode observed in the M2 case is again more visible due to the structure's higher spatial interaction. Thus, the study qualitatively confirms the role of cross-coupling as a new mechanism for achieving sensing feedback within a nanostructure. The non-resonant detection along the tail of the resonance spectrum is also expected to achieve linear sensing performance under such random morphological states [65].

4. Conclusion

To recapitulate, we experimentally implement a modified abstraction of Sierpiński fractals of order 1 and 2 such that we achieve specific functionalities of the state-of-the-art bow-tie nanostructures, namely (i) improved dipolar resonance contrast, (ii) optical magnetism in a new kind of split-ring like configurations and (iii) non-resonant

detection of a weak fingerprint of an ultra-thin film followed by a cross-coupling mediated sensing of the morphological transformation of the film. The enhanced contrast of the dipolar mode is meaningful for microfluidic surface enhanced infrared absorption spectroscopy in the presence of strong water absorption loss whereas the generation of magnetic modes can push the operating wavelength to far-IR and beyond in a given footprint. Furthermore, we systematically exploit the lightning rod effect of the sharp metal corners in the fractalized bow-tie structures for both engineering of the resonance characteristics and enhancement of electric field interaction in the non-resonant regime. Using this concept, we successfully demonstrate strong coupling to the molecular modes at non-resonant regime even under critical thermal broadening. Complex plasmonic systems are getting ubiquitous as the building block for exotic optical properties such as frequency independence [66] and ultrafast electron-photon coupling [67]. Here, we report a major advancement in the sensing application of fractal plasmonics by successfully realizing a set of reverse engineered, rationally modified and rather complex nano-architectures. The detection of monolayer fingerprint in the non-resonant regime will undoubtedly extend the bandwidth of plasmonic nanostructures for complete profiling of mid-IR characteristics when integrated with biological elements and eliminate the need for off-chip solution by attenuated total internal reflection spectroscopy (ATR). The study clearly unveils the fact that the second order fractal design is more effective to track molecular signal from random ensemble due to its larger electric field enhancement and increased spatial overlap. We also believe that, the proposed fractal inspired nano-architectures combining spatially and spectrally variant yet mutually coupled modes will pursue a new avenue for multiplexed colorimetric detection of stochastic events in biomedical and forensic applications. It is also expected that the complex nano-architectures can be expanded to higher degrees on a large scale with the advancement of nanotechnology in the near future.

Author contributions

The manuscript was written with contributions from all authors. All authors have given approval to the final version of the manuscript.

Acknowledgments

The authors acknowledge the financial support from the research grants of: CRP—AlN (R-263-000-C24-281); NRF-ISF (R-263-000-C64-281); A*STAR-NCBR (R-263-000-C91-305) and the National Natural Science Foundation of China under Grant No. 61474078 at NUS (Suzhou) Research Institute, Suzhou, China.

ORCID iDs

Chengkuo Lee https://orcid.org/0000-0002-8886-3649

References

[1] Baliarda C P, Romeu J and Cardama A 2000 The Koch monopole: a small fractal antenna *IEEE Trans. Antennas Propag.* **48** 1773–81
[2] Mordechai S, Marin S and John M D 2012 Fractal optics and beyond *Nat. Photon.* **6** 209–10
[3] Xu X, Hasan D, Wang L, Chakravarty S, Chen R T, Fan D L and Wang A X 2012 Guided mode-resonance-coupled plasmonic-active SiO_2 nanotubes for surface enhanced Raman spectroscopy *Appl. Phys. Lett.* **100** 191114
[4] Xu X, Li H, Hasan D, Ruoff R S, Wang A X and Fan D L 2013 Near-field enhanced plasmonic-magnetic bifunctional nanotubes for single cell bioanalysis *Adv. Funct. Mater.* **23** 4332–8
[5] Ren F, Campbell J, Hasan D, Wang X, Rorrer G and Wang A 2013 Bio-inspired plasmonic sensors by diatom frustules *CLEO CTh3I.4*
[6] Hasan D and Shah Alam M 2014 Ultra-broadband confinement in deep sub-wavelength air hole of a suspended core fiber *J. Lightwave Technol.* **32** 1434–41
[7] Hasan M M, Kumar D S, Mahdy M R C, Hasan D N and Matin M A 2013 Robust optical fiber using single negative metamaterial cladding *IEEE Photon. Technol. Lett.* **25** 1043–6
[8] Hasan D, Ho C P, Pitchappa P and Lee C 2015 Dipolar resonance enhancement and magnetic resonance in cross-coupled bow-tie nanoantenna array by plasmonic cavity *ACS Photon.* **2** 890–8
[9] Karker N, Dharmalingam G and Carpenter M A 2014 Thermal energy harvesting plasmonic based chemical sensors *ACS Nano.* **8** 10953–62
[10] Dregely D, Lindfors K, Lippitz M, Engheta N, Totzeck M and Giessen H 2014 Imaging and steering an optical wireless nanoantenna link *Nat. Commun.* **5** 4354
[11] Volpe G, Volpe G and Quidant R 2011 Fractal plasmonics: subdiffraction focusing and broadband spectral response by a Sierpinski nanocarpet *Opt. Express* **19** 3612–8
[12] Afshinmanesh F, Curto A G, Milaninia K M, Van Hulst N F and Brongersma M L 2014 Transparent metallic fractal electrodes for semiconductor devices *Nano Lett.* **14** 5068–74
[13] Abdellatif S and Kirah K 2013 Nanowire photovoltaic efficiency enhancement using plasmonic coupled nano-fractal antennas *Opt. Lett.* **38** 3680–3
[14] Luchowski R, Shtoyko T, Matveeva E, Sarkar P, Borejdo J, Gryczynski Z and Gryczynski I 2010 Molecular fluorescence enhancement on fractal-like structures *Appl. Spectrosc.* **64** 578–83
[15] Kazerooni H and Khavasi A 2014 Plasmonic fractals: ultrabroadband light trapping in thin film solar cells by a Sierpinski nanocarpet *Opt. Quantum Electron.* **46** 751–7

[16] Gottheim S, Zhang H, Alexander O G and Halas N J 2015 Fractal nanoparticle plasmonics: the cayley tree *ACS Nano.* **9** 3284–92
[17] Falconer K 2005 *Fractal Geometry: Mathematical Foundations and Applications* vol 2 (New York: Wiley) pp 27–38
[18] Pan L *et al* 2011 Maskless plasmonic lithography at 22 nm resolution *Sci. Rep.* **1** 1–6
[19] Roxworthy B J, Ko K D, Kumar A, Fung K H, Chow E K C, Liu G L, Fang N X and Toussaint K C 2012 Application of plasmonic bowtie nanoantenna arrays for optical trapping, stacking, and sorting *Nano Lett.* **12** 796–801
[20] Kinkhabwala A, Yu Z, Fan S, Avlasevich Y, Müllen K and Moerner W E 2009 Large single-molecule fluorescence enhancements produced by a bowtie nanoantenna *Nat. Photon.* **3** 654–7
[21] Sivis M, Duwe M, Abel B and Ropers C 2013 Extreme-ultraviolet light generation in plasmonic nanostructures *Nat. Phys.* **9** 304–9
[22] Roxworthy B J, Bhuiya A M, Inavalli V V, Chen H and Toussaint K C 2014 Multifunctional plasmonic film for recording near-field optical intensity *Nano Lett.* **14** 4687–93
[23] Cakmakyapan S, Cinel N A, Cakmak A O and Ozbay E 2014 Validation of electromagnetic field enhancement in near-infrared through Sierpinski fractal nanoantennas *Opt. Express* **22** 19504–12
[24] Gramotnev D K and Bozhevolnyi S I 2014 Nanofocusing of electromagnetic radiation *Nat. Photon.* **8** 13–22
[25] Qian J, Liu C, Wang W, Chen J, Li Y, Xu J and Sun Q 2013 Effect of edge rounding on the extinction properties of hollow metal nanoparticles *Plasmonics.* **8** 955–62
[26] Raziman T V and Martin O J F 2013 Polarisation charges and scattering behaviour of realistically rounded plasmonic nanostructures *Opt. Express* **21** 21500–7
[27] Ibella P, Neubrech F, Huck C, Golmar F, Casanova F, Hueso L E, Pucci A, Aizpurua J and Hillenbrand R 2013 Experimental verification of the spectral shift between near- and far-field peak intensities of plasmonic infrared nanoantennas *Phys. Rev. Lett.* **110** 203902
[28] Zuloaga J and Nordlander P 2011 On the energy shift between near-field and far-field peak intensities in localized plasmon systems *Nano Lett.* **11** 1280–3
[29] Menzel C, Hebestreit E, Mühlig S, Rockstuhl C, Burger S, Lederer F and Pertsch T 2014 The spectral shift between near- and far-field resonances of optical nano-antennas *Opt. Express* **22** 9971–82
[30] Pendry J B, Holden A J, Robbins D J and Stewart W J 1999 Magnetism from conductors and enhanced nonlinear phenomena microwave theory and techniques *IEEE Trans. On.* **47** 2075–84
[31] Linden S, Enkrich C, Wegener M, Zhou J, Koschny T and Soukoulis C M 2004 Magnetic response of metamaterials at 100 Terahertz *Science* **306** 1351
[32] Hein S M and Giessen H 2013 Tailoring magnetic dipole emission with plasmonic split-ring resonators *Phys. Rev. Lett.* **111** 026803
[33] Denkova D *et al* 2013 Mapping magnetic near-field distributions of plasmonic nanoantennas *ACS Nano* **7** 3168–76
[34] Aigouy L, Cazé A, Gredin P, Mortier M and Carminati R 2014 Mapping and quantifying electric and magnetic dipole luminescence at the nanoscale *Phys. Rev. Lett.* **113** 076101
[35] Pitchappa P, Ho C P, Lin Y, Kropelnicki P, Huang C, Singh N and Lee C 2014 Micro-electro-mechanically tunable metamaterial with enhanced electro-optic performance *Appl. Phys. Lett.* **104** 151104
[36] Pitchappa P, Ho C P, Kropelnicki P, Singh N, Kwong D and Lee C 2014 Dual band complementary metamaterial absorber in near infrared region *J. Appl. Phys.* **115** 193109
[37] Ho C P, Pitchappa P, Lin Y, Huang C, Kropelnicki P and Lee C 2014 Electrothermally actuated microelectromechanical systems based Omega-ring terahertz metamaterial with polarization dependent characteristics *Appl. Phys. Lett.* **104** 1611040
[38] Ma F, Lin Y, Zhang X and Lee C 2014 Tunable multiband terahertz metamaterials using a reconfigurable electric split-ring resonator array *Light: Sci. Appl.* **3**
[39] Pitchappa P, Ho C P, Qian Y, Dhakar L, Singh N and Lee C 2015 Microelectromechanically tunable multiband metamaterial with preserved isotropy *Sci. Rep.* **5** 1–10
[40] Roxworthya B J and Toussaint K C 2014 Simultaneously tuning the electric and magnetic plasmonic response using capped bi-metallic nanoantennas *Nanoscale* **6** 2270–4
[41] Lin E, Tsai W, Lee K, Lee M M and Wei P 2014 Enhancing detection sensitivity of metallic nanostructures by resonant coupling mode and spectral integration analysis *Opt. Express* **22** 19621–32
[42] Adato R, Aksu S and Altug H 2015 Engineering mid-infrared nanoantennas for surface enhanced infrared absorption spectroscopy *Mater. Today* **00** 11
[43] Shafiei F, Monticone F, Le K Q, Liu X, Hartsfield T, Li X and Alu A 2013 A subwavelength plasmonic metamolecule exhibiting magnetic-based optical Fano resonance *Nat. Nanotechnol.* **8** 95–100
[44] Aizpurua J, Bryant G W, Richter L J, García de Abajo F J, Kelley B K and Mallouk T 2005 Optical properties of coupled metallic nanorods for field-enhanced spectroscopy *Phys. Rev.* B **71** 235420
[45] Brown L V, Yang X, Zhao K, Zheng B Y, Nordlander P and Halas N J 2015 Fan-shaped gold nanoantennas above reflective substrates for surface-enhanced infrared absorption (SEIRA) *Nano Lett.* **15** 1272–80
[46] Zhu D, Bosman M and Yang J K W 2014 A circuit model for plasmonic resonators *Opt. Express* **22** 9809–19
[47] Corrigan T D, Kolb P W, Sushkov A B, Drew H D, Schmadel D C and Phaneuf R J 2008 Optical plasmonic resonances in split-ring resonator structures: an improved LC model *Opt. Express* **16** 19850–64
[48] Koh A L, Andez-Domínguez F, McComb D W, Maier S A and Yang J K W 2011 High-resolution mapping of electron-beam-excited plasmon modes in lithographically defined gold nanostructures *Nano Lett.* **11** 1323–30
[49] Wang W, Christensen T, Jauho A, Thygesen K S, Wubs M and Asger Mortensen N 2015 Plasmonic eigenmodes in individual and bow-tie graphene nanotriangles *Sci. Rep.* **5** 9535
[50] Prodan E, Radloff C, Halas N J and Nordlander P A 2003 Hybridization model for the plasmon response of complex nanostructures *Science* **302** 419–22
[51] Berkovitch N and Orenstein M 2011 Thin wire shortening of plasmonic nanoparticle dimers: the reason for red shifts *Nano Lett.* **11** 2079–82
[52] Lahiri B, McMeekin S G, De La Rue R M and Johnson N P 2013 Enhanced Fano resonance of organic material films deposited on arrays of asymmetric split-ring resonators (A-SRRs) *Opt. Express* **21** 9343–52
[53] Shelton D J, Brener I, Ginn J C, Sinclair M B, Peters D W, Coffey K R and Boreman G D 2011 Strong coupling between nanoscale metamaterials and phonons *Nano Lett.* **11** 2104–8
[54] Alici K B and Gallardo I F 2013 Detecting secondary structure and surface orientation of helical peptide monolayers from resonant hybridization signals *Sci. Rep.* **3** 2956
[55] Dregely D, Neubrech F, Duan H, Vogelgesang R and Giessen H 2013 Vibrational near-field mapping of planar and buried three-dimensional plasmonic nanostructures *Nat. Commun.* **4** 2237

[56] Grefe S E, Leiva D, Mastel S, Dhuey S D, Cabrini S, Schuckc P J and Abate Y 2013 Near-field spatial mapping of strongly interacting multiple plasmonic infrared antennas *Phys. Chem. Chem. Phys.* **15** 18944
[57] Adato R, Yanik A A, Wu C, Shvets G and Altug H 2010 Radiative engineering of plasmon lifetimes in embedded nanoantenna arrays *Opt. Express* **18** 4526–37
[58] Verma A and Sharma A 2010 Enhanced self-organized dewetting of ultrathin polymer films under water-organic solutions: fabrication of sub-micrometer spherical lens arrays *Adv. Mater.* **22** 5306–9
[59] Kargupta K and Sharma A 2002 Dewetting of thin films on periodic physically and chemically patterned surfaces *Langmuir* **18** 1893–903
[60] Gentili D, Foschi G, Valle F, Cavallini M and Biscarini F 2012 Applications of dewetting in micro and nanotechnology *Chem. Soc. Rev.* **41** 4430–43
[61] Kang M, Park S-G and Jeong K-H 2015 Repeated solid-state dewetting of thin gold films for nanogap-rich plasmonic nanoislands *Sci. Rep.* **5** 14790
[62] Huck C, Vogt J, Sendner M, Hengstler D, Neubrech F and Pucci A 2015 Plasmonic enhancement of infrared vibrational signals: nanoslits versus nanorods *ACS Photon.* **2** 1489–97
[63] Rieppo L *et al* 2012 Application of second derivative spectroscopy for increasing molecular specificity of fourier transform infrared spectroscopic imaging of articular cartilage *Osteoarthritis Cartilage* **20** 451–9
[64] Cheng F, Yang X and Gao J 2015 Ultrasensitive detection and characterization of molecules with infrared plasmonic metamaterials *Sci. Rep.* **5** 14327
[65] Yakovlev V V, Dickson W, Murphy A, McPhillips J, Pollard R J, Podolskiy V A and Zayats A V 2013 Ultrasensitive non-resonant detection of ultrasound with plasmonic metamaterials *Adv. Mater.* **25** 2351–6
[66] Zuani S D, Reindl T, Rommel M, Gompf B, Berrier A and Dressel M 2015 High-order hilbert curves: fractal structures with isotropic, tailorable optical properties *ACS Photon.* **2** 1719–24
[67] Zhong L, Jiang Y, Liow C, Meng F, Sun Y, Chandran B K, Liang Z, Jiang L, Li S and Chen X 2015 Electro-plasmonic switches: highly sensitive electro-plasmonic switches based on fivefold stellate polyhedral gold nanoparticles *Small* **11** 5329–401